

Wet Chemical Synthesis and Optical Properties of Co²⁺-Doped Magnesium Stannate Ceramics

E. B. da Silva Junior^a, A. López^a, S. S. Pedro^{a*} , L. P. Sosman^a 

^aUniversidade do Estado do Rio de Janeiro, Instituto de Física, 20550-013, Rio de Janeiro, RJ, Brasil.

Received: November 07, 2023; Revised: February 01, 2024; Accepted: February 14, 2024

Magnesium stannate (Mg₂SnO₄) samples with 0.003, 0.004, 0.03, 0.05, 0.08, 0.1, 0.2, 0.3, 0.5, 1, 2, and 5 at. mol% of Co²⁺ were prepared by wet chemical method. The samples were investigated using X-Ray diffraction and photoluminescence techniques at room temperature. The results indicate that Co²⁺ occupies tetrahedral sites in the inverse spinel structure of Mg₂SnO₄, replacing Mg²⁺. The material exhibited a red-infrared luminescence associated with Co²⁺ spin-allowed transitions. Crystal field parameters were calculated using Tanabe-Sugano theory for d⁷ systems in tetrahedral environment. In the range studied, optimum divalent cobalt concentration for emission applications was found to be 0.08 at. mol%.

Keywords: Ceramics, Optical Materials, Chemical Synthesis, Optical Properties, Luminescence.

1. Introduction

Magnesium stannate ceramics (Mg₂SnO₄) is a very versatile host from the point of view of optical properties, due to its inverse spinel structure. Such structure consists of octahedral and tetrahedral sites, which makes its doping with transition metal (TM) and rare earth (RE) cations of different valences possible. Depending on the position of the cation inserted in the system, the material can emit luminescence. In the case of a TM doping, the emission can occur in the visible and near infrared (originated from the transition metal occupation in tetrahedral sites), or in the infrared (through the transition metal occupation in octahedral sites). From the point of view of spectroscopic properties, this characteristic opens the possibility of obtaining emission from the material in different wavelengths, enabling the generation of systems in tunable frequency bands.

Based in these characteristics, several works report the synthesis of Mg₂SnO₄ in diverse ways and with varied doping. The most common preparation method is the solid-state route^{1,2}, but other methods were also described, such as sol-gel auto-combustion³, modified Pechini method⁴, millimeter-wave heating⁵ and co-precipitation method⁶.

Undoped Mg₂SnO₄ presents a persistent luminescence in the visible range, widely known and investigated. Several works report an intense band between 400-500 nm under UV excitation^{3,7}. The origin of this emission is associated with lattice defects and oxygen vacancies, which generates electron or hole traps. The recombination of F centers (negative oxygen vacancies) with holes causes the luminescence observed in the blue-green region^{7,8}.

Concerning the doped system, we can find in literature works reporting this host containing transition metals as activators, such as Mn²⁺^{5,9}, exhibiting a green luminescence,

with emission in the same region of the undoped Mg₂SnO₄; Fe³⁺, with a near-infrared broadband in the 720-789 nm range¹⁰; Cr³⁺, also generating a near-infrared band with persistent luminescence characteristics^{11,12}; and a Cr³⁺ and Ni²⁺ co-doped system, resulting in a super broadband in the near-infrared in the 830-1480 nm range¹³. However, there are very few works that explore the doping of the material with divalent cobalt ions and with specific focus on its optical properties. Our research group previously synthesized the Mg₂SnO₄ with 0.1 at. mol% of Co²⁺ through solid state reaction. The emission spectra exhibited two bands, the most intense in the 650-780 nm range, accompanied by a weak band in 800-900 nm region. These bands were assigned to Co²⁺ transitions in tetrahedral sites¹⁴.

In addition to the optical properties, several authors have already demonstrated that Mg₂SnO₄ has diverse applications, such as dielectric material for microwave devices¹, electronic ceramics¹⁵, wireless high-temperature sensor¹⁶, field emission displays (FEDs)¹⁷, self-sustainable night vision devices¹⁰, Li-ion battery electrodes (when combined with SnO₂)¹⁸, probe in autofluorescence bioimaging¹¹, fingerprint visualization¹⁹ and optical storage⁸.

In this work, we successfully performed the synthesis of the magnesium stannate containing several concentrations of the divalent cobalt cation, using the wet chemical method, commonly used in the synthesis of superconductor materials²⁰, but little explored in the production of light-emitting ceramics^{21,22}. The technique consists of a coprecipitation from an aqueous solution of acetic acid containing metal ions, followed by a calcination at high temperature after evaporation of organic compounds from the solution. The structure of the material was investigated using the X-ray diffraction technique and Rietveld refinement. Optical properties were investigated using photoluminescence emission and excitation spectroscopy, in addition to radiative lifetime measurements.

*e-mail: sandrapedro@uerj.br

2. Experimental

2.1. Material synthesis

Specimens of magnesium stannate Mg_2SnO_4 ($2\text{MgO}:1\text{SnO}_2$) with several Co^{2+} concentrations were prepared using the wet chemical route²⁰⁻²². This method consists in the stoichiometric mixture of the powder oxides MgO (99.0%, Riedel-de Haen), SnO_2 (99.9%, Sigma-Aldrich) and CoCO_3 (99.0%, Coleman & Bell) in a solution containing 50% of glacial acetic acid ($\text{CH}_3\text{CO}_2\text{H}$) diluted in 50% of distilled water. The masses of the raw materials were calculated to produce a set of samples doped nominally with 0.003, 0.004, 0.03, 0.05, 0.08, 0.1, 0.2, 0.3, 0.5, 1, 2, and 5 at. mol% of Co^{2+} , replacing Mg^{2+} ions. Since MgO is highly hygroscopic, this reagent was used in excess of 10% related to its mass calculated in the stoichiometry. A solution containing distilled water and acetic acid was placed together with the powder reagents in a beaker, mixed and slowly heated over a heat plate to evaporate the liquid. Then, the resulting mixture was put in an oven at 100 °C for 24 hours. Next, the solid mixture was placed in an alumina crucible and calcinated in a muffle furnace at a temperature of 700 °C during 6 hours for removal of organic waste. The calcinated mixture was macerated for 10 minutes to obtain a fine powder.

The powder was divided equally in three parts to make three pellets for each sample. Each part was axially pressed under 3400 Kgf/cm² and it were obtained pellets with 13 mm in diameter and 2 mm in thickness. These pellets were placed in alumina crucibles and put in a muffle furnace for 10 hours at 1250 °C in air. At the end of 10 h, the oven was turned off and the pellets were cooled to room temperature by thermal inertia and then removed from the oven. Samples exhibited colors varying from light blue (almost white) to sky blue, according to Co^{2+} increasing concentration, as can be seen on Figure 1.

2.2. Material characterization

Samples were subjected to crystal structure analysis and phase identification through investigation by powder X-ray diffraction (XRD) technique. One pellet of each concentration was grounded in an agate mortar for XRD measurements. Diffraction patterns were obtained using a Bruker D2 Phaser diffractometer with $\text{Cu-K}\alpha_1$ radiation ($\lambda = 1.54056 \text{ \AA}$) operating at 30 kV and 10 mA. Data were collected in a Bragg–Brentano geometry with $10^\circ < 2\theta < 65^\circ$ and 0.01° step size. XRD data were refined using the Rietveld method through the *FullProf* Suite package²³. Refinement was executed using data from the Inorganic Crystal Structure Database (ICSD) as starting point. Rietveld refinement provides information regarding

the space group, lattice parameters, and phase quantification, among other parameters.

Photoluminescence experiments (emission (PL), excitation (PLE), and time emission decay) were performed at room temperature (RT) using a PTI 300 *QuantaMaster* spectrofluorometer equipped with a 75 W pulsed xenon with a repetition rate of 200 Hz. Wavelength scans were performed with a step increment set at 1 nm, variable slit widths, and signal detection obtained using a PTI 914 photomultiplier detection system (185–900 nm range, peak at 400 nm). Newport filters were used to block the excitation wavelengths and scattered light in the emission-detection apparatus. All optical spectra were corrected using the apparatus sensitivity response.

3. Results and Discussion

3.1. Crystal structure

Figure 2 displays the room temperature diffraction pattern of all samples. Rietveld refinement was executed in every diffractogram, using *FullProf* software and data from cubic Mg_2SnO_4 as starting point (ICSD code 28199). The refinement result can also be seen on Figure 2, where red dots are the experimental data, the black line is the calculated pattern obtained from refinement, and the Mg_2SnO_4 Bragg reflections are positioned below the diffractograms (green, purple and orange sticks). The bottom line in blue is the difference between the experimental and calculated XRD patterns. The χ^2 showed in the Figure 2 for each sample indicates that the observed XRD experimental patterns agree closely with the calculated refinements. The sharp peaks indicate that all samples have high crystallinity. The most intense peaks are indexed as Mg_2SnO_4 single phase. The DRX patterns did not change significantly with Co^{2+} doping as can be seen on Figure 2.

In these diffractograms the Mg_2SnO_4 main phase is accompanied by small amounts of unreacted MgO or SnO_2 with phase proportions lower than 5%, depending on sample. In Figure 2 the asterisks point to the peaks related to the MgO and SnO_2 phases. The appearance of these unreacted compounds is usual since both are highly hygroscopic. Due to the small proportion of these secondary phases, they are not expected to affect the photoluminescent properties of the studied samples.

In MgO the Mg ion is in an octahedral site, and it is known that the Co^{2+} ions have a preference by tetrahedral sites. However, statistically is not expected that Co^{2+} ions occupy Mg sites in MgO. In similar form, in SnO_2 Sn^{4+} ions are in octahedral sites. Moreover, the valences difference (Co^{2+} and Sn^{4+}) are not favorable for Co-Sn substitution.



Figure 1. Samples after thermal treatment. From left to right, the Co^{2+} concentration increases at the following order: 0.003, 0.004, 0.03, 0.05, 0.08, 0.1, 0.2, 0.3, 0.5, 1, 2 and 5 at. mol% of Co^{2+} .

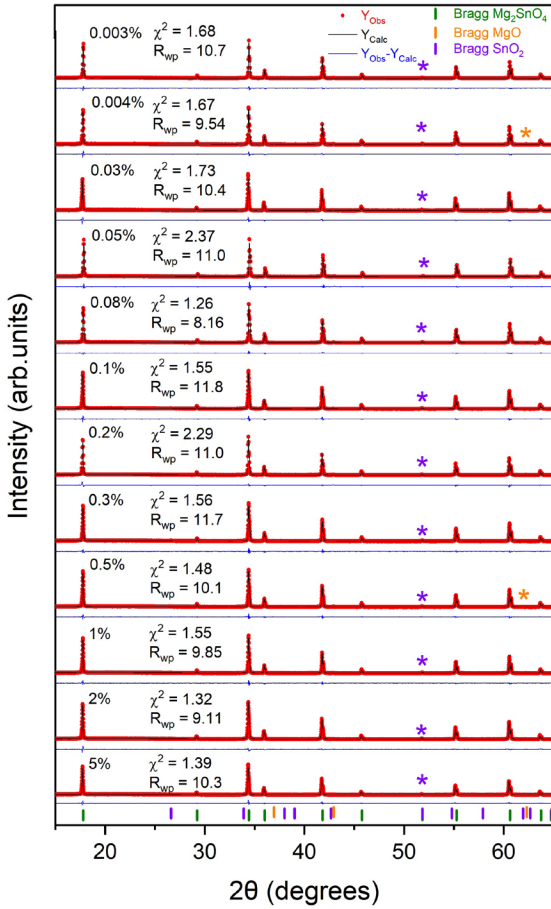


Figure 2. XRD pattern and Rietveld refinement for all samples. Experimental data are represented by red circles while the black line represents the calculated profile. The difference between the calculated and observed data is represented by the blue line. Green sticks represent Mg₂SnO₄ Bragg reflections, purple sticks SnO₂ Bragg reflections and orange sticks MgO Bragg reflections. Asterisks point to the peaks related to the SnO₂ (purple) and MgO (orange) phases.

A discussion about the valence of the cations inserted in the host lattice can be made based on the X-ray results shown in Figure 2. It is expected that, using enough cobalt reagent in the sample preparation, a crystalline phase will emerge in which Co is a host cation. Considering the possibility of Co²⁺ oxidizing to Co³⁺, the expected phase would be MgCo₂O₄ spinel in which the Co³⁺ ions would be in octahedral sites. The X-ray data does not indicate the presence of MgCo₂O₄ in none of the studied samples. Therefore, Co³⁺ ions are not expected in these samples.

Table 1 presents the main crystallographic parameters extracted from the Rietveld refinement for the sample with 0.1 at mol% of Co²⁺ and Table 2 presents the coordinates of the atomic positions also extracted from the refinement. The main phase Mg₂SnO₄ (99.66% in phase proportion) presents an inverse spinel structure, with tetrahedral (A) and octahedral (B) sites, space group *Fd3m*. The unit cell has a cubic symmetry containing 8 A, 16 B and 32 oxygen atoms^{7,9,24}. Mg²⁺ ions are found in both A and B sites, but Sn⁴⁺ occupy only B positions. According to the refinement, the lattice parameter is $a = 8.632(7)$ Å. In this sample, SnO₂

Table 1. Refined crystallographic parameters and agreement factors for 0.1 at. mol% of Co²⁺ sample.

Sample	0.1 at mol.% of Co ²⁺
	Mg ₂ SnO ₄
ICSD code	28199
Phase Proportion (%)	99.66
Crystal System	Cubic
Space Group	<i>Fd3m</i>
$a = b = c$ (Å)	8.632(7)
α, β, γ (°)	90, 90, 90
Cell Volume (Å ³)	643.3(6)
	SnO ₂
ICSD Code	9009082
Phase Proportion (%)	0.34
Crystal System	Cubic
Space Group	<i>P4₂/mm</i>
$a = b, c$ (Å)	4.735(3), 3.183(6)
α, β, γ (°)	90, 90, 90
Cell Volume (Å ³)	71.3(8)
	Agreement factors
R_{wp}	11.8
R_p	10.9
R_{exp}	8.61
χ^2	1.55
GOF-index	1.2

Table 2. Mg₂SnO₄ main phase and SnO₂ secondary phase atomic positions for the 0.1 at. mol% of Co²⁺ sample.

Cation	Ox State	Wyck Symbol	x	y	z	Occ
Mg ₂ SnO ₄						
Mg1	+2	8 a	0.00000	0.00000	0.00000	0.04167
Mg2	+2	16 d	0.62500	0.62500	0.62500	0.04167
Sn1	+4	16 d	0.62500	0.62500	0.62500	0.04167
O1	-2	32 e	0.38355	0.38355	0.38355	0.16667
SnO ₂						
Sn1	+4	16 d	0.00000	0.00000	0.00000	0.12500
O1	-2	32 e	0.28422	0.28422	0.00000	0.25000

has only 0.34% in phase proportion according to refinement. The Co²⁺ doping up to 5% did not change significantly the Mg₂SnO₄ crystal structure.

The ionic radii of Mg²⁺ (0.57 Å/ 0.72 Å, CN = 4/6) and Sn⁴⁺ (0.69 Å, CN = 6), where CN = coordination number, are compared with Co²⁺ (0.58 Å/ 0.74 Å, CN = 4/6, high spin) in tetrahedral environment²⁵, and we can observe that these values are very similar. However, it is believed that

the divalent cobalt cations tend to occupy Mg^{2+} tetrahedral positions, due to their valence similarity¹⁴. Photoluminescence measurements can help to clarify which site (octahedral or tetrahedral) is preferential for Co^{2+} occupation and can also be used to confirm the valence of the emitting cation. These results are presented in next section.

3.2. Photoluminescence spectroscopy

The photoluminescence spectra of the Co^{2+} -doped samples in the 600-900 nm range, under 560 nm excitation wavelength and slit width of 3 nm, are exhibited in Figure 3. All spectra present a broad, homogeneous band in the red-

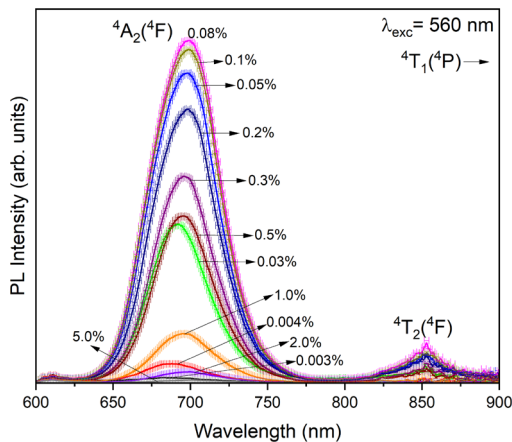


Figure 3. Photoluminescence spectra of the Co^{2+} -doped samples under 560 nm excitation at room temperature.

infrared range, with emission intensity varying with Co^{2+} doping level. A weak structure is also observed around 853 nm. These bands are identified as Co^{2+} emission in tetrahedral sites, where the band in higher energy is assigned to the ${}^4T_1(4P) \rightarrow {}^4A_2(4F)$ spin-allowed transition. The weak structure at 853 nm is assigned to the ${}^4T_1(4P) \rightarrow {}^4T_2(4F)$ Co^{2+} spin-allowed transition. Similar spectra were also obtained when the same compound containing 0.1 at. mol% of Co^{2+} was synthesized via solid state route, exhibiting a broad band peaked at 698 nm under 500 nm excitation¹⁴. Other authors working with systems using Co^{2+} as activator report similar spectra^{26,27}.

The divalent cobalt concentration plays an important role in the emission intensity. In this way, Figure 4 depicts the changes of relative integrated intensity, the wavelength position of the band maximum (band peak) and the FWHM (full width at half maximum) as a function of Co^{2+} doping level. From Figure 3 and Figure 4a we can observe that in the investigated range, the sample with 0.08 at mol% of Co^{2+} is the concentration which presented the most intense spectrum and highest relative integrated intensity, very close to the 0.1 at mol% of Co^{2+} . For higher concentrations, the relative integrated intensity of emission decreases. The bands shape does not change significantly with concentration, but there is a slight change in the band maximum (band peak, see Figure 4b).

In Figures 4b and 4c is shown the band peak and FWHM of selected samples. The samples with 0.003, 0.004, 2, and 5 at. mol% of Co^{2+} are not shown due to its low intensity. The 0.08 at. mol% of Co^{2+} sample has a band peak at 697

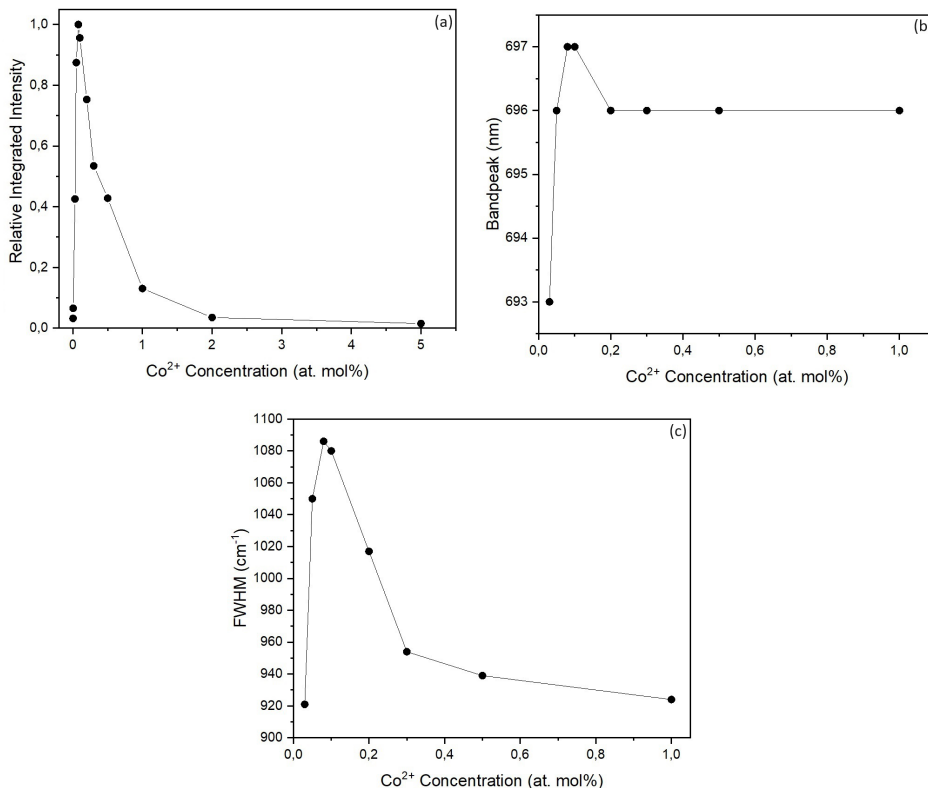


Figure 4. Samples' emission characteristics as a function of Co^{2+} doping concentration. (a) Relative Integrated Intensity; (b) Band peak and (c) FWHM.

nm, which does not change significantly in the 0.05 - 1.0 at. mol% of Co²⁺ range. In this range, the band peak is found in the 696-698 nm. This shift of ± 1 nm is not significant, since it is within the range of the slit used in the measurements (3 nm). In addition, the bands are homogeneous. The homogeneous broadening and similar shape of the strongest emission bands indicate that Co²⁺ occupies only one kind of site in the 0.05%-1% at. mol% of Co²⁺ concentration range. The photoluminescence results did not show evidence of the presence of cobalt with a valence other than +2.

Full width at half maximum (FWHM) is a good parameter to describe whether an emission has the potential to be tunable. The greater the FWHM, the greater the ability of an emission to be tunable over a wide spectral range. Figure 4c shows the FWHM for selected samples, and it is found that this parameter increases until it reaches a maximum value for the 0.08 at. mol% of Co²⁺ sample, which has a FWHM of 1086 cm⁻¹ (52 nm). For higher concentrations, the FWHM decreases. Based in these results, it is possible to affirm that the 0.08 at. mol% of Co²⁺ sample presents the best emission characteristics, with the most intense emission and the wider FWHM. In addition, in the studied samples, a concentration quenching occurs above 0.08 at. mol% of Co²⁺, where the emission decreases as an effect of increasing Co²⁺ concentration, causing the absorption of the emission by their neighbors.

For a concentration quenching situation it is possible to estimate the critical distance R_c according to Dexter-Schulman theory. Considering the energy transfer process between two identical emitting centers, the critical distance can be defined as the distance for which the transfer probability equals the emission probability^{28,29}. The value of R_c can be calculated from Equation 1:

$$R_c = 2 \left(\frac{3V}{4\pi x_c n} \right)^{1/3} \quad (1)$$

where V is the volume of the unit cell, x_c is the critical concentration and n is the number of lattice sites in the unit cell that can be occupied by the Co²⁺³¹. For our sample set, $x_c = 0.0008$, $V = 643 \text{ \AA}^3$ and $n = 8$, which gives $R_c = 58 \text{ \AA}$.

The value of R_c indicates which mechanism is predominant in the energy transfer process. If the critical distance is less than 5 \AA , exchange interaction is predominant. For greater values of R_c , the energy transfer process is mainly governed by multipolar interactions³⁰⁻³³, which is the case of Mg₂SnO₄:Co²⁺. According to Dexter-Schulman theory, the relationship between the emission intensity and the activator concentration can be expressed as Equation 2^{30,31,33}:

$$\log(I/x) = \log(K) - \log(\beta) - (\theta/3)\log(x) \quad (2)$$

where x is the activator concentration, and I/x is the emission integrated intensity per activator concentration (x). K and β are constants. Typical values of θ are 3 (nearest-neighbor interaction), 6 (dipole-dipole interaction), 8 (dipole-quadrupole interaction) and 10 (quadrupole-quadrupole interaction)^{30,31,33-35}.

The plot of $\log(I/x)$ as a function of $\log(x)$ for the band in higher energy in the 0.08-5 at. mol% of Co²⁺ concentration range^{35,36} is exhibited in Figure 5. The slope of the plot is related to the $\theta/3$ value. In this way, the slope of 2.14897

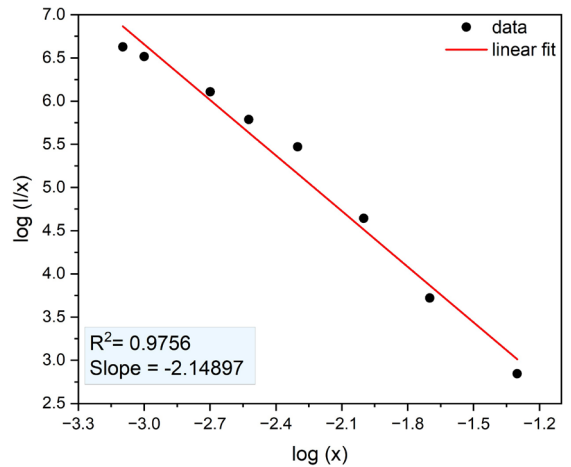


Figure 5. Plot of $\log(I/x)$ versus $\log(x)$ for Mg₂SnO₄:Co²⁺.

gives a θ value of 6.4 which is approximately equal to 6. This result indicates that the main process governing the concentration quenching in Mg₂SnO₄:Co²⁺ is the dipole-dipole interaction.

Transition-metal Co²⁺ presents the d⁷ electronic configuration. The structures observed in the optical spectra can be related to the electronic transitions using Tanabe-Sugano theory³⁷⁻³⁹. From the energies associated with the observed transitions in the emission spectra and using the Tanabe-Sugano matrices for d⁷ electronic configuration, the values of the crystal field parameter (Dq) and Racah parameter (B) can be calculated. Using these Tanabe-Sugano matrices it was obtained the following parameters: crystal field $Dq = 252-285 \text{ cm}^{-1}$ (depending on the Co²⁺ concentration) and $B = 782 \text{ cm}^{-1}$, with Dq/B in the 0.32-0.37 range (see Table 3). The values found for the energy parameters are in concordance with other systems containing Co²⁺ as activator with weak crystal field in tetrahedral coordination^{22,40}. The value of the B Racah parameter is lower than the free ion value (971 cm^{-1})⁴¹, which indicates that the Co²⁺-O²⁻ bond has a covalent character.

Figure 6 depicts the Co-doped photoluminescence excitation spectra (PLE) for selected samples monitored at 715 nm. The spectra have similar features, with the structures related to electronic transitions of Co²⁺ inserted in tetrahedral sites. Structures identified at 560 nm (17857 cm^{-1}), 600 nm (16667 cm^{-1}) and 660 nm (15151 cm^{-1}) are assigned to the $^4A_2(^4F) \rightarrow ^2A_1(^2G)$, $^4A_2(^4F) \rightarrow ^2E(^2G)$ and $^4A_2(^4F) \rightarrow ^4T_1(^4P)$ electronic transitions, respectively. The transitions observed in the PLE spectra indicate that the transition positions do not depend on Co²⁺ concentration level.

Co²⁺ energy levels in Mg₂SnO₄ identified in PL and PLE spectra for 0.08 at. mol% of Co²⁺ sample are presented in Figure 7. The order of the energy levels is determined by the ratio Dq/B . For the Dq/B values found (see Table 3), which were related to a weak crystal field, the ground level is the $^4A_2(^4F)$, followed by $^4T_2(^4F)$, $^4T_1(^4P)$, $^2E(^2G)$ and $^2A_1(^2G)$.

According to the energy level diagram, divalent cobalt electrons are excited by visible light leaving the $^4A_2(^4F)$ ground level and occupy the $^4T_1(^4P)$, $^2E(^2G)$ and $^2A_1(^2G)$ excited levels. After some time, these electrons decay via a

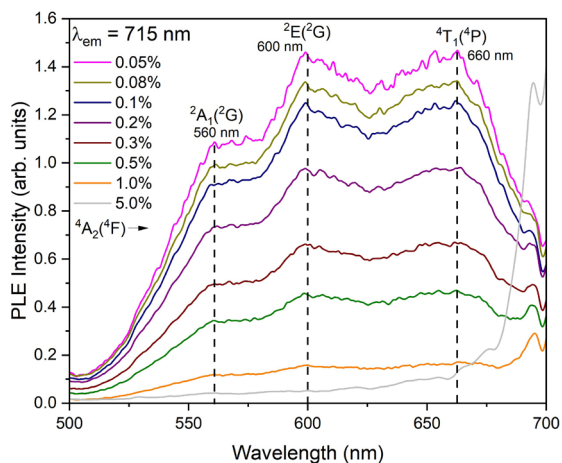


Figure 6. Excitation spectra as a function of Co^{2+} doping concentration.

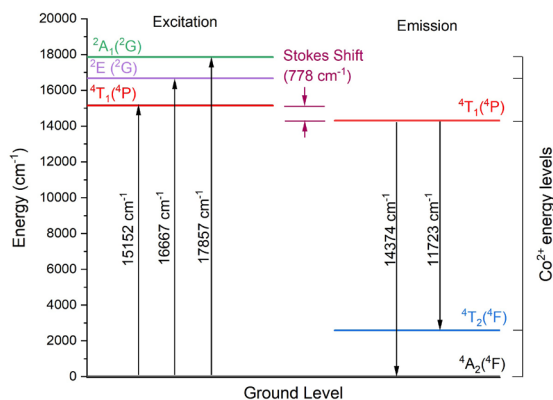


Figure 7. Energy levels of $\text{Mg}_2\text{SnO}_4:\text{Co}^{2+}$ (0.08 at mol% of Co^{2+}).

Table 3. Crystal field parameters.

Concentration (at. mol% Co^{2+})	Dq (cm^{-1})	B (cm^{-1})	Dq/B
0.003	285	782	0.37
0.004	279	782	0.36
0.03	271	782	0.35
0.05	264	782	0.34
0.08	262	782	0.34
0.1	262	782	0.34
0.2	264	782	0.34
0.3	264	782	0.34
0.5	264	782	0.34
1.0	264	782	0.34
2.0	260	782	0.33
5.0	252	782	0.32

nonradiative process to the ${}^4\text{T}_1({}^4\text{P})$ level, losing part of the initial energy to lattice vibrations. This energy difference between the excitation and emission processes related to the ${}^4\text{T}_1({}^4\text{P})$ level is called Stokes shift. For 0.08 at. mol% of Co^{2+} sample the Stokes shift is $\Delta S = 778 \text{ cm}^{-1}$. This value of the Stokes shift is considered short, and it was found similar for the 0.1 at. mol% of Co^{2+} sample (770 cm^{-1}) obtained by solid state reaction for this group, leading to a self-absorption process and possible interference from

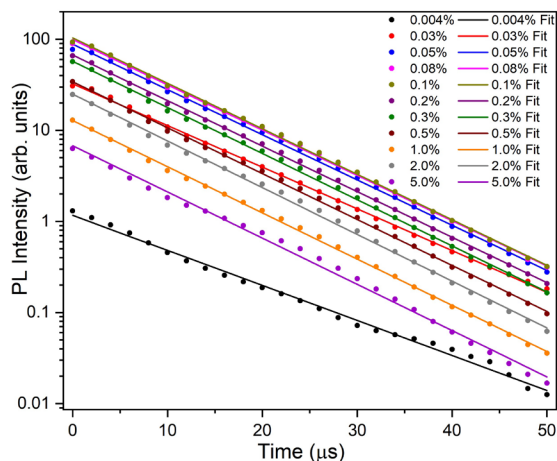


Figure 8. Time decay curves of Mg_2SnO_4 for several Co^{2+} concentrations (at. mol%). Dots are experimental data, and the lines are the linear fitting of experimental data. The curves were obtained with emission positioned at 715 nm under 630 nm excitation.

Table 4. Time decays obtained from fitting.

Concentration (at. mol% Co^{2+})	τ (μs)
0.004	11.3
0.03	9.4
0.05	8.7
0.08	8.7
0.1	8.7
0.2	8.7
0.3	8.6
0.5	8.6
1.0	8.6
2.0	8.5
5.0	8.6

excitation wavelengths in the sample emission¹⁴. Due to this considerable overlapping, the proximity among Co^{2+} ions could lead to a marked luminescence quenching when the Co^{2+} level increases above a specific limit which will depend on the kind of occupation site. In these samples, due to the increasing of Co^{2+} concentration, the distance between neighborhood Co^{2+} ions decrease leading to quenching effect, which is clearly observed in Figure 4a.

Figure 8 exhibits the time decay curves using 630 nm excitation for ${}^4\text{T}_1({}^4\text{P}) \rightarrow {}^4\text{A}_2({}^4\text{F})$ transition at 715 nm. Experimental data (represented as dots in the Figure 8) were fitted using a single exponential profile. From the fitting, the radiative lifetime for all samples can be seen on Table 4. The radiative time decay helps to identify the nature of the transition related to the emission process. Emission related to spin-forbidden transitions are associated to higher time decays while spin-allowed transitions have a lower time decay⁴². In general, ceramics containing divalent cobalt in tetrahedral sites as an activator have a short decay time originated by spin-allowed transitions.

The observed short radiative lifetimes close to 9 μs is like other Co^{2+} -doped systems and associated to spin-allowed electric dipole transitions, which corroborates the transition assignment related to the emission spectra^{14,22}. Moreover,

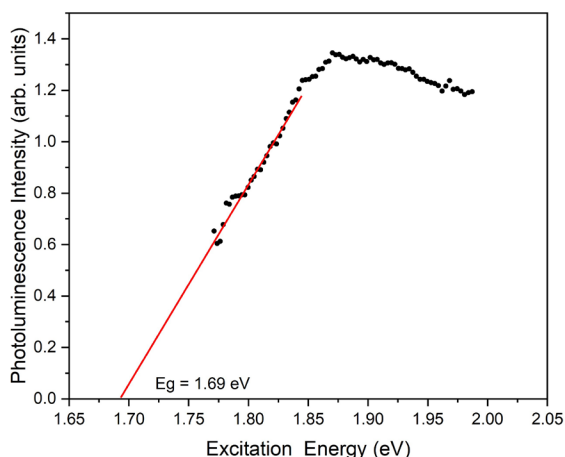


Figure 9. Bandgap estimative from PLE data. Black circles are experimental data extracted from 0.08 at. mol% of Co²⁺ excitation spectrum and the red line is the extrapolation from PLE data. The bandgap is estimated at 1.69 eV.

the results indicated that the time decay does not change significantly with divalent cobalt doping. As reduction of the emission lifetime with Co²⁺ level increasing is not observed, it is possible to affirm that the energy transfer Co²⁺-Co²⁺ or from Co²⁺ to any other luminescence quencher site is not significant in the investigated concentration range.

Concerning the bandgap, the best experimental data to estimate this property comes from the spectra obtained from absorption spectroscopy. Unfortunately, absorption spectroscopy measurements were not performed in this work due the lack of the appropriate experimental setup. Despite this, it is known that usually the absorption bands are similar in energy and shape to the photoluminescence excitation bands (PLE). This was previously observed for several spinels such as MgGa₂O₄:Co²⁺^{43,44}, ZnGa₂O₄:Co²⁺^{44,45}, and MgGa₂O₄:Cr³⁺⁴⁶.

Some authors showed results of bandgap calculation using PLE instead of UV-VIS absorption spectroscopy with results close to those obtained with absorption spectroscopy⁴⁷⁻⁵⁰. In this way, considering the possibility of the similarity between PLE and absorption spectra of the Mg₂SnO₄:Co²⁺, as seen in references⁴³⁻⁴⁵, the bandgap value for the Mg₂SnO₄:Co²⁺ of the most emitting sample (0.08 at mol% of Co²⁺) was estimated from PLE spectra. Figure 9 shows the low energy side of the PLE spectrum (black circle). The bandgap is determined by a linear extrapolation of the PLE data (the linear fitting is the red solid line). As the low energy side of spectrum does not extend up to horizontal axis, the bandgap value E_g = 1.69 eV is roughly estimated. Considering that the spectra for all samples have a similar profile, it is expected that the bandgap values be similar for all samples in the 0.05 – 1 at. mol % of Co²⁺ range.

4. Conclusions

Mg₂SnO₄ ceramics containing several Co²⁺ concentrations in the 0.003 - 5 at. mol% of Co²⁺ concentration range were synthesized by wet chemical route. To our knowledge, it is the first time that this material was synthesized using this preparation method. Samples were investigated through

XRD, PL and PLE techniques. The XRD patterns did not change significantly with Co²⁺ level. Rietveld refinement confirms the presence of the main phase Mg₂SnO₄ in all samples accompanied by small amounts of MgO and SnO₂. PL spectra exhibit emission in the red / near-infrared for all samples with a more intense band in the 650-750 nm range accompanied by a weaker band in the 800-900 nm range. The analysis of the emission features for all samples indicated that the 0.08 at. mol% of Co²⁺ sample has the best results, with the highest integrated intensity and largest FWHM. The photoluminescence results did not show evidence of the presence of cobalt with a valence other than +2. The integrated intensity emission as a function of the activator concentration indicates that the dipole-dipole interaction is the mechanism that rules the concentration quenching. PL and PLE spectra are characteristic of Co²⁺ in tetrahedral environment. Based in the optical spectra, the crystal field parameters Dq and B were calculated. Time decay calculations confirm the assignment of the bands. The estimated bandgap for the most emitting sample was 1.69 eV. The results obtained indicate that Mg₂SnO₄:Co²⁺ has potential for application as a tunable source in the infrared region at room temperature.

5. Acknowledgments

This study was financed in part by the Coordenação de Aperfeiçoamento de Pessoal de Nível Superior - Brasil (CAPES) - Finance Code 001. The authors are also grateful to Fundação de Amparo à Pesquisa do Estado do Rio de Janeiro (FAPERJ) and Financiadora de Estudos e Projetos (FINEP) for their financial support. The authors also thank LIETA-UERJ, Brazil for X-ray diffraction measurements. L. P. Sosman and S. S. Pedro thank Conselho Nacional de Desenvolvimento Científico e Tecnológico (CNPq) for their Research Productivity fellowships. S. S. Pedro thanks FAPERJ for the Jovem Cientista do Nosso Estado (JCNE) fellowship.

6. References

- Chen YC, Li CH. Improving quality factor of Mg₂SnO₄ ceramics by removing moisture content from starting raw materials. *Ceram Int.* 2016;42(8):9749-51. <http://dx.doi.org/10.1016/j.ceramint.2016.03.066>.
- Azad AM, Min LJ. Mg₂SnO₄ ceramics I. Synthesis-processing-microstructure correlation. *Ceram Int.* 2001;27(3):325-34. [http://dx.doi.org/10.1016/S0272-8842\(00\)00085-7](http://dx.doi.org/10.1016/S0272-8842(00)00085-7).
- Tsega M, Dejene FB. Photoluminescence and thermoluminescence properties of sol-gel auto-combustion driven Mg₂SnO₄ nanophosphor. *ECS J Solid State Sci Technol.* 2018;7(11):R183-9. <http://dx.doi.org/10.1149/2.0161811jsss>.
- Costa JM, Lima LC, Li MS, Santos IMG, Silva MRS, Maia AS. Structural and photocalalytic properties of Mg₂SnO₄ spinel obtained by modified Pechini method. *Mater Lett.* 2019;236:320-3. <http://dx.doi.org/10.1016/j.matlet.2018.10.129>.
- Kitaura M, Tani S, Mitsudo S, Fukui K. Photoluminescence enhancement in manganese-doped magnesium stannate phosphors synthesized by millimeter-wave irradiation. *Radiat Meas.* 2010;45(3-6):503-5. <http://dx.doi.org/10.1016/j.radmeas.2010.01.024>.
- Tang H, Cheng C, Yu G, Liu H, Chen W. Structure and electrochemical properties of Mg₂SnO₄ nanoparticles synthesized by a facile co-precipitation method. *Mater Chem Phys.* 2015;159:167-72. <http://dx.doi.org/10.1016/j.matchemphys.2015.03.066>.

7. Zhang J, Yu M, Qin Q, Zhou H, Zhou M, Xu X, et al. The persistent luminescence and up conversion photostimulated luminescence properties of nondoped Mg_2SnO_4 material. *J Appl Phys*. 2010;108(12):123518. <http://dx.doi.org/10.1063/1.3524280>.
8. Zhang JC, Qin QS, Yu MH, Sun JY, Shi LR, Ma XL. Up-conversion photostimulated luminescence of Mg_2SnO_4 for optical storage. *Chin Phys Lett*. 2011;28(2):027802. <http://dx.doi.org/10.1088/0256-307X/28/2/027802>.
9. Kim KN, Jung HK, Park HD, Kim D. High luminance of new green emitting phosphor $\text{Mg}_2\text{SnO}_4:\text{Mn}$. *J Lumin*. 2002;99(3):169-73. [http://dx.doi.org/10.1016/S0022-2313\(02\)00334-4](http://dx.doi.org/10.1016/S0022-2313(02)00334-4).
10. Li M, Jin Y, Yuan L, Wang B, Wu H, Hu Y, et al. Near-infrared long afterglow in Fe^{3+} -Activated Mg_2SnO_4 for Self-sustainable night vision. *ACS Appl Mater Interfaces*. 2023;15(10):13186-94. <http://dx.doi.org/10.1021/acsmi.3c00673>.
11. Xie W, Jiang W, Zhou R, Li J, Ding J, Ni H, et al. Disorder-induced broadband near-infrared persistent and photostimulated luminescence in $\text{Mg}_2\text{SnO}_4:\text{Cr}^{3+}$. *Inorg Chem*. 2021;60(4):2219-27. <http://dx.doi.org/10.1021/acs.inorgchem.0c02941>.
12. Zhou Z, He F, Song E, Zhang S, Yi X, Zhang H, et al. Broadband and multimode near-infrared emitter based on Cr^{3+} -activated stannate for multifunctional applications. *Adv Opt Mater*. 2023;11(7):2202466. <http://dx.doi.org/10.1002/adom.202202466>.
13. Liu BM, Guo XX, Huang L, Zhou RF, Zou R, Ma CG, et al. A super-broadband NIR dual-emitting $\text{Mg}_2\text{SnO}_4:\text{Cr}^{3+}, \text{Ni}^{2+}$ phosphor for ratiometric phosphor-converted NIR light source applications. *Adv Mater Technol*. 2023;8(4):2201181. <http://dx.doi.org/10.1002/admt.202201181>.
14. Silva EB Jr, Lopez A, Pedro SS, Sosman LP. Photoluminescence of Co^{2+} ions in Mg_2SnO_4 tetrahedral sites. *Opt Mater*. 2019;95:109202. <http://dx.doi.org/10.1016/j.optmat.2019.109202>.
15. Al-Shahrani AA. Sintering behavior and thermal property of Mg_2SnO_4 . *J Mater Sci Mater Electron*. 2005;16(4):193-6. <http://dx.doi.org/10.1007/s10854-005-0764-3>.
16. Liao YT, Chen YC, Kuo CC. Millimeter-wave passive patch antenna for use in wireless high-temperature sensor. *Sens Mater*. 2022;34(6):2281-92. <http://dx.doi.org/10.18494/SAM3841>.
17. Li G, Zhang X, Peng C, Shang M, Geng D, Cheng Z, et al. Cyan-emitting Ti^{4+} - and Mn^{2+} -coactivated Mg_2SnO_4 as a potential phosphor to enlarge the color gamut for field emission display. *J Mater Chem*. 2011;21(18):6477-9. <http://dx.doi.org/10.1039/c1jm00057h>.
18. Xiao T, Tang Y, Jia Z, Feng S. Synthesis of $\text{SnO}_2/\text{Mg}_2\text{SnO}_4$ nanoparticles and their electrochemical performance for use in Li-ion battery electrodes. *Electrochim Acta*. 2009;54(8):2396-401. <http://dx.doi.org/10.1016/j.electacta.2008.10.061>.
19. Xue J, Hu T, Li F, Liu F, Noh HM, Lee BR, et al. Suppressed self-reduction of manganese in Mg_2SnO_4 via Li^+ incorporation with polychromatic luminescence for versatile applications. *Laser Photonics Rev*. 2023;17(4):2200832. <http://dx.doi.org/10.1002/lpor.202200832>.
20. Itoh T, Uchikawa H. Preparation of the superconductor $\text{YBa}_2\text{Cu}_3\text{O}_x$ from an aqueous solution of acetic acid containing metal ions. *J Mater Sci Lett*. 1988;7(7):693-4. <http://dx.doi.org/10.1007/BF00722069>.
21. da Silva MAFM, Pedro SS, Lopez A, Sosman LP. Investigation on the structural and photoluminescent properties of chromium-doped cordierite. *Opt Mater*. 2016;60:188-95. <http://dx.doi.org/10.1016/j.optmat.2016.07.033>.
22. Santos RD, Pedro SS, López A, Sosman LP. Preparation, structural properties and tunable photoluminescence of $\text{LiZnNbO}_4:\text{Co}^{2+}$. *J Lumin*. 2017;185:55-60. <http://dx.doi.org/10.1016/j.jlumin.2017.01.009>.
23. Roisnel T, Rodriguez-Carvajal J. Fullprof Suite Program Fullprof.2k V. 4.80 Laboratoire Leon Brillouin (CEA-CNRS) [Internet]. 2010 [cited 2023 Nov 7]. Available from: <http://www.ill.eu/sites/fullprof/index.html>
24. Lei B, Lin B, Wang X, Li W. Green emitting long lasting phosphorescence (LLP) properties of $\text{Mg}_2\text{SnO}_4:\text{Mn}^{2+}$ phosphor. *J Lumin*. 2006;118(2):173-8. <http://dx.doi.org/10.1016/j.jlumin.2005.08.010>.
25. Shannon RD. Revised effective ionic radii and systematic studies of interatomic distances in halides and chalcogenides. *Acta Crystallogr A*. 1976;A32(5):751-67. <http://dx.doi.org/10.1107/S0567739476001551>.
26. Belyaev A, Basyrova L, Sysoev V, Lelet M, Balabanov S, Kalganov V, et al. Microstructure, doping and optical properties of $\text{Co}^{2+}:\text{ZnAl}_2\text{O}_4$ transparent ceramics for saturable absorbers: effect of the ZnF_2 sintering additive. *J Alloys Compd*. 2020;829:154514. <http://dx.doi.org/10.1016/j.jallcom.2020.154514>.
27. Dymshits O, Vitkin V, Alekseeva I, Khubetsov A, Tsenter M, Polishchuk A, et al. Transparent glass-ceramics based on Co^{2+} -doped $\gamma\text{-Ga}_x\text{Al}_{2-x}\text{O}_3$ spinel nanocrystals for passive Q-switching of Er lasers. *J Lumin*. 2021;234:117993. <http://dx.doi.org/10.1016/j.jlumin.2021.117993>.
28. Dexter DL, Schulman JH. Theory of concentration quenching in inorganic phosphors. *J Chem Phys*. 1965;22(6):1063-70. <http://dx.doi.org/10.1063/1.1740265>.
29. Blasse G. Energy transfer in oxidic phosphors. *Phys Lett A*. 1968;28A(6):444-5. [http://dx.doi.org/10.1016/0375-9601\(68\)90486-6](http://dx.doi.org/10.1016/0375-9601(68)90486-6).
30. Chen Y, Guo Q, Liao L, He M, Zhou T, Mei L, et al. Preparation, crystal structure and luminescence properties of a novel single-phase red emitting phosphor $\text{CaSr}_2(\text{PO}_4)_2:\text{Sm}^{3+}, \text{Li}^+$. *RSC Adv*. 2019;9(9):4834-42. <http://dx.doi.org/10.1039/C9RA00264B>.
31. Hebbar DN, Menon SG, Choudhari KS, Shivashankar SA, Santhosh C, Kulkarni SD. Cr-doped ZnAl_2O_4 : microwave solution route for ceramic nanoparticles from metalorganic complexes in minutes. *J Am Ceram Soc*. 2018;101(2):800-11. <http://dx.doi.org/10.1111/jace.15256>.
32. Yan Y, Huo H, Zhang H, Zhao T, Wang Q, Zou X, et al. Preparation and luminescence of Dy^{3+} doped glass-ceramics containing ZnMoO_4 . *J Non-Cryst Solids*. 2021;569:120990. <http://dx.doi.org/10.1016/j.jnoncrysol.2021.120990>.
33. Liu J, Zhao W, Liu J, Gao H, Hao B. Luminescent properties of new red emitting fluoroborate based phosphors, $\text{Na}_3\text{Ba}_2-x\text{B}_6\text{O}_{12}\text{F}_x\text{Eu}^{3+}$. *Optik*. 2019;179:427-33. <http://dx.doi.org/10.1016/j.ijleo.2018.10.148>.
34. Ozawa L, Jaffe M. The mechanism of the emission color shift with activator concentration in Eu^{3+} activated phosphors. *J Electrochem Soc*. 1971;118(10):1678-9. <http://dx.doi.org/10.1149/1.2407810>.
35. Zhang W, Chen Y, Geng X, Yang Y, Xiao L. Synthesis and luminescence properties of $\text{LiBaB}_9\text{O}_{15}:\text{Eu}^{3+}$ single-component red-light emitting phosphors. *J Lumin*. 2020;224:117324. <http://dx.doi.org/10.1016/j.jlumin.2020.117324>.
36. Sowjanya G, Daddoji R, Reddy VRM. Structural, luminescence, energy transfer mechanism, and properties of Sm^{3+} -doped KYBO phosphors. *Radiat Phys Chem*. 2022;190:109791. <http://dx.doi.org/10.1016/j.radphyschem.2021.109791>.
37. Tanabe Y, Sugano S. On the absorption spectra of complex ions. I. *J Phys Soc Jpn*. 1954;9(5):753-66. <http://dx.doi.org/10.1143/JPSJ.9.753>.
38. Tanabe Y, Sugano S. On the absorption spectra of complex ions. II. *J Phys Soc Jpn*. 1954;9(5):766-79. <http://dx.doi.org/10.1143/JPSJ.9.766>.
39. Tanabe Y, Sugano S. On the absorption spectra of complex ions. III. The calculation of the crystalline field strength. *J Phys Soc Jpn*. 1956;11(8):864-77. <http://dx.doi.org/10.1143/JPSJ.11.864>.
40. Espinoza VAA, López A, Neumann R, Sosman LP, Pedro SS. Photoluminescence of divalent cobalt ions in tetrahedral sites of zinc orthotitanate. *J Alloys Compd*. 2017;720:417-22. <http://dx.doi.org/10.1016/j.jallcom.2017.05.188>.

41. Henderson B, Bartram RH. Crystal-field engineering of solid-state laser materials. Cambridge: Cambridge University Press, 2000. <http://dx.doi.org/10.1017/CBO9780511524165>.
42. Renero-Lecuna C, Martín-Rodríguez R, Gonzalez JA, Rodríguez F, Almonacid G, Segura A, et al. Photoluminescence in ZnO:Co²⁺ (0.01%-5%) nanoparticles, nanowires, thin films, and single crystals as a function of pressure and temperature: exploring the electron-phonon interactions. *Chem Mater*. 2014;26(2):1100-7. <http://dx.doi.org/10.1021/cm403371n>.
43. Sosman LP, Abritta T, Pereira AC, Vargas H. Photoacoustic spectroscopy of Co²⁺ in ZnGa₂O₄ and MgGa₂O₄. *Chem Phys Lett*. 1994;227(4-5):485-9. [http://dx.doi.org/10.1016/0009-2614\(94\)00856-6](http://dx.doi.org/10.1016/0009-2614(94)00856-6).
44. Sosman LP, Abritta T. Optical spectroscopy of MgGa₂O₄:Co²⁺. *Solid State Commun*. 1992;82(10):801-3. [http://dx.doi.org/10.1016/0038-1098\(92\)90168-9](http://dx.doi.org/10.1016/0038-1098(92)90168-9).
45. Abritta T, Blak FH. Luminescence study of ZnGa₂O₄:Co²⁺. *J Lumin*. 1991;48-49:558-60. [http://dx.doi.org/10.1016/0022-2313\(91\)90192-X](http://dx.doi.org/10.1016/0022-2313(91)90192-X).
46. Sosman LP, Abritta T, Nakamura O, D'Aguiar MMF No. Luminescence and photoacoustic study of MgGa₂O₄: Cr³⁺. *Phys Status Solidi, A Appl Res*. 1995;147(2):K107-10. <http://dx.doi.org/10.1002/pssa.2211470246>.
47. Monemar B. Fundamental energy gap of GaN from photoluminescence excitation spectra. *Phys Rev, B, Solid State*. 1974;10(2):676-81. <http://dx.doi.org/10.1103/PhysRevB.10.676>.
48. Roura P, López-de-Miguel M, Cornet A, Morante JR. Determination of the direct band-gap energy of InAlAs matched to InP by photoluminescence excitation spectroscopy. *J Appl Phys*. 1997;81(10):6916-20. <http://dx.doi.org/10.1063/1.365253>.
49. Bleuse J, Perret S, Curé Y, Grenet L, André R, Mariette H. Optical determination of the band gap and band tail of epitaxial Ag₂ZnSnSe₄ at low temperature. *Phys Rev B*. 2020;102(19):19505. <http://dx.doi.org/10.1103/PhysRevB.102.195205>.
50. Qiao L, Xiao HY, Meyer HM, Sun JN, Rouleau CM, Puztzky AA, et al. Nature of the band gap and origin of the electro-/photo-activity of Co₃O₄. *J Mater Chem C Mater Opt Electron Devices*. 2013;1(31):4628-33. <http://dx.doi.org/10.1039/c3tc30861h>.